

## HIGH ANGULAR RESOLUTION OBSERVATIONS OF FOUR CANDIDATE BLAST HIGH-MASS STARLESS CORES

LUCA OLMI<sup>1,2</sup>, ESTEBAN D. ARAYA<sup>3</sup>, EDWARD L. CHAPIN<sup>4</sup>, ANDREW GIBB<sup>4</sup>, PETER HOFNER<sup>5,6,7</sup>, PETER G. MARTIN<sup>8,9</sup>,  
AND CARLOS M. POVENTUD<sup>1</sup>

<sup>1</sup> Physics Department, Rio Piedras Campus, University of Puerto Rico, Box 23343, UPR Station, San Juan, Puerto Rico, USA;  
[olmi.luca@gmail.com](mailto:olmi.luca@gmail.com), [olmi@arcetri.astro.it](mailto:olmi@arcetri.astro.it)

<sup>2</sup> INAF, Osservatorio Astrofisico di Arcetri, Largo E. Fermi 5, I-50125, Firenze, Italy

<sup>3</sup> Physics Department, Western Illinois University, 1 University Circle, Macomb, IL 61455, USA

<sup>4</sup> Department of Physics & Astronomy, University of British Columbia, 6224 Agricultural Road, Vancouver, BC V6T 1Z1, Canada

<sup>5</sup> Physics Department, New Mexico Institute of Mining and Technology, 801 Leroy Place, Socorro, NM 87801, USA

<sup>6</sup> NRAO, P.O. Box O, 1003 Lopezville Road, Socorro, NM 87801-0387, USA

<sup>7</sup> Max-Planck-Institut für Radioastronomie, Auf dem Hügel 69, 53121 Bonn, Germany

<sup>8</sup> Canadian Institute for Theoretical Astrophysics, University of Toronto, 60 St. George Street, Toronto, ON M5S 3H8, Canada

<sup>9</sup> Department of Astronomy & Astrophysics, University of Toronto, 50 St. George Street, Toronto, ON M5S 3H4, Canada

Received 2010 January 22; accepted 2010 April 13; published 2010 May 6

### ABSTRACT

We discuss high angular resolution observations of ammonia toward four candidate high-mass starless cores (HMSCs). The cores were identified by the Balloon-borne Large Aperture Submillimeter Telescope (BLAST) during its 2005 survey of the Vulpecula region where 60 compact sources were detected simultaneously at 250, 350, and 500  $\mu\text{m}$ . Four of these cores, with no *IRAS*–PSC or *MSX* counterparts, were mapped with the NRAO Very Large Array and observed with the Effelsberg 100 m telescope in the  $\text{NH}_3(1,1)$  and  $(2,2)$  spectral lines. Our observations indicate that the four cores are cold ( $T_k < 16$  K) and show a filamentary and/or clumpy structure. They also show a significant velocity substructure within  $\sim 1$  km s<sup>−1</sup>. The four BLAST cores appear to be colder and more quiescent than other previously observed HMSC candidates, suggesting an earlier stage of evolution.

*Key words:* balloons – ISM: clouds – ISM: molecules – radio lines: ISM – stars: formation – submillimeter: ISM

*Online-only material:* color figures

### 1. INTRODUCTION

The importance of massive ( $M \gtrsim 8 M_\odot$ ) stars in shaping the Galactic structure and evolution is well known (Zinnecker & Yorke 2007). In recent years, a major observational effort has been made to identify the earliest stages of their evolution, which are not very well constrained, yet. Systematic studies by various groups have uncovered several high-mass proto-stellar objects (HMPOs), i.e., dense gravitationally bound cores in a pre-ultracompact (UC) H II region phase with typical temperatures  $T \sim 15$ –90 K (Molinari et al. 1996, 2002; Sridharan et al. 2002; Beuther et al. 2002).

However, these surveys were carried out on *IRAS*-selected objects and thus there are very few observations of the so-called high-mass starless (or pre-protostellar) core (HMSC) stage, which is supposed to precede the HMPO phase, and their physical and kinematical properties have been barely studied. The survey by Sridharan et al. (2005) was also based on previous observations of *IRAS*-selected candidate HMPOs at 1.2 mm, thus quite far from the emission peak of the spectral energy distribution (SED) of the coldest ( $T \lesssim 15$  K) cores. The survey of infrared dark clouds (IRDCs) by Pillai et al. (2006) showed that IRDCs are cold ( $T < 20$  K), massive ( $M > 100 M_\odot$ ), and have linewidths  $\simeq 1$ –3 km s<sup>−1</sup>. However, these authors probed regions with typical sizes  $\gtrsim 1$  pc, thus likely to represent pre-protoclusters. Motte et al. (2007) in their unbiased survey of Cygnus X found 17 cores qualifying as good candidates for hosting massive IR-quiet protostars, driving outflows traced by SiO emission, but failed to discover the high-mass analogs of pre-stellar dense cores.

Detailed studies of individual objects (e.g., G28.34+0.06, Wang et al. 2008; Zhang et al. 2009; *IRAS* 05345+3157, Fontani et al. 2009; Cygnus X, Bontemps et al. 2009) are

now contributing to set further constraints on the fragmentation inside massive dense clumps, leading to individual collapsing protostars. These works have tentatively identified cores in very early evolutionary stages, which make them good targets to study the initial fragmentation phases in molecular clumps. In this paper, we describe four massive cores that appear to be even colder and more quiescent than similar objects observed in previous works, and may thus further constitute excellent targets for follow-up studies on the initial fragmentation phases.

The Balloon-borne Large Aperture Submillimeter Telescope (BLAST) has recently identified a new and unique sample of massive, cold dust clumps, with characteristics sizes  $\lesssim 0.4$  pc. BLAST is a 2 m stratospheric balloon telescope that observes simultaneously at 250, 350, and 500  $\mu\text{m}$  using bolometric imaging arrays (Pascale et al. 2008). BLAST, until the first Galactic results from *Herschel* become available, is unique in its ability to detect and characterize cold dust emission from both starless and protostellar sources, constraining the temperatures of objects with  $T \lesssim 25$  K using its three-band photometry near the peak of the cold core SED. During the first BLAST science flight (BLAST 05), BLAST conducted the first sensitive large-scale Galactic Plane surveys at these wavelengths.

One of the regions observed by BLAST05 covered 4 deg<sup>2</sup> near the open cluster NGC 6823 in the constellation Vulpecula ( $\ell = 59^\circ$ ), at a distance of about 2.3 kpc (see the discussion in Chapin et al. 2008). In this region, 60 compact sources ( $< 60''$  diameter) were detected simultaneously in all three bands. Their SEDs were constrained through BLAST, *IRAS*, *Spitzer* MIPS, and *MSX* photometry, with inferred dust temperatures spanning  $\sim 12$ –40 K assuming a dust emissivity index  $\beta = 1.5$ , and total masses  $\sim 15$ –700  $M_\odot$  (Chapin et al. 2008). At least 30% of these cores are new, with no *IRAS*–PSC or *MSX* associations. Even then, most of those with *IRAS* identifications have not

**Table 1**  
VLA Observing Parameters

BLAST ID	Source Name	R.A.[J2000]	Decl.[J2000]	Synthesized Beam (arcsec)	Sensitivity (mJy beam <sup>-1</sup> )
V10	BLAST J194106+235513	19:41:06.5	+23:55:13.5	3.3 × 2.9	4.7
V11	BLAST J194136+232325	19:41:36.3	+23:23:24.9	3.3 × 2.8	4.3
V27	BLAST J194306+230125	19:43:06.5	+23:01:25.5	3.4 × 2.7	4.4
V33	BLAST J194319+232639	19:43:19.0	+23:26:39.6	3.4 × 3.0	5.9

**Notes.** The coordinates represent the BLAST core peak positions and VLA phase tracking center. The synthesized beam and sensitivity refer to the NH<sub>3</sub>(1,1) line.

been studied in detail. The sources detected in the BLAST bands, in particular those without *IRAS* counterparts, indicate the presence of significant quantities of cool dust. Thus, the BLAST observations resulted in a unique and uniform sample, which may contain a number of *bona fide* HMSCs.

Among the 60 compact BLAST sources, we selected the four coldest, massive, and IR-quiet cores (see Section 2.1) for observations with the NRAO<sup>10</sup> Very Large Array (VLA) in the NH<sub>3</sub>(1,1) and (2,2) spectral lines. The structure of the paper is thus the following: we describe the observations and discuss the main results in Section 2. Our analysis is presented in Section 3, and finally our conclusions are summarized in Section 4.

## 2. OBSERVATIONS AND DATA REDUCTION

### 2.1. The Sample

Among the starless cores candidates in Vulpecula, i.e., with no *IRAS*–PSC or *MSX* counterparts, we selected the four coldest ( $T_{\text{dust}} < 16$  K) BLAST sources, V10, V11, V27, and V33 (see Table 1), to be observed with the VLA. An analysis of *Spitzer* IRAC and MIPS images reveals that only source V11 might have an associated protostar, as we discuss later (Section 3.5).

These cores are also massive (with envelope masses  $\sim 90$ – $200 M_{\odot}$ ) and both their absolute luminosities ( $L_{\text{FIR}} \sim 50 L_{\odot}$ ) and luminosity-to-mass ratios ( $L_{\text{FIR}}/M \lesssim 1 L_{\odot} M_{\odot}^{-1}$ ; see Figure 18 of Chapin et al. 2008) suggest an early phase of evolution. Qualitatively, this can also be seen by positioning the four sources in the  $L$ – $M$  diagram of Molinari et al. (2008; see their Figure 9), where they would fall in the region representing the early accretion phase. On the same diagram, it can be seen that these BLAST cores are clearly separated from the low-mass regime.

None of the selected sources in Vulpecula are listed in the catalog of Extended Green Objects (EGOs) of Cyganowski et al. (2008), a sample of massive young stellar objects outflow candidates extracted from the GLIMPSE survey (Benjamin et al. 2003). Among the Vulpecula sources that fall in the GLIMPSE survey area (which include V10, V11, V27, and V33) only V09 qualifies as an EGO. This is yet another indication of the early evolutionary phase of the BLAST cores in our sample.

These four Vulpecula cores were observed with the VLA in the NH<sub>3</sub>(1,1) and (2,2) spectral lines, which are low-excitation molecular lines, thus appropriate to study the cold cores in the BLAST catalog. In addition, the NH<sub>3</sub> molecule is not expected to be much depleted in pre-stellar cores (e.g., Aikawa et al. 2005), although its exact abundance may depend on the core density (Tafalla et al. 2002; Flower et al. 2006).

### 2.2. VLA Observations

The VLA ammonia observations were carried out in 2008 June, and the array was used in its most compact configuration (D), with baselines from 35 m to 1 km. The NH<sub>3</sub>(1,1) and (2,2) inversion lines at 23.694496 and 23.722633 GHz, respectively (Ho & Townes 1983), were simultaneously observed in the 1IF mode, with a bandwidth of 6.25 MHz and 128 channels, corresponding to a velocity coverage of about 80 km s<sup>-1</sup> and a velocity resolution of about 0.6 km s<sup>-1</sup>. The mapped area in each source was  $\simeq 2.5 \times 2.5$ , centered around the nominal positions of the BLAST cores shown with crosses in Figures 1–6, and with a synthesized beam FWHM  $\simeq 3$  arcsec (see Table 1). The total time on-source varied from  $\simeq 30$  to  $\simeq 40$  minutes per source and per line. The flux density scale was established by observing 3C48 and the phase calibration was ensured by frequent observations of the point source J19259+21064, that had a measured flux density at the time of the observations of 2.1 Jy. The data were edited and calibrated using the Astronomical Image Processing System (AIPS) following standard procedures. Imaging and deconvolution was performed using the IMAGR task and naturally weighting the visibilities. The resulting observing parameters are listed in Table 1.

In order to derive the rotation temperature (Section 3.1) we also need to convert the VLA spectra in units of temperature. The conversion from flux per beam to brightness temperature measured in the synthesized beam,  $T_{\text{sb}}$ , is obtained using the relation (at the frequency of the NH<sub>3</sub>(1,1) line)

$$T_{\text{sb}} \text{ (K)} = 2.18 \frac{F_{\nu} \text{ (mJy beam}^{-1}\text{)}}{\theta_{\text{min}} \text{ ("}\text{)} \theta_{\text{max}} \text{ ("}\text{)}}, \quad (1)$$

where  $\theta_{\text{min}}$  and  $\theta_{\text{max}}$  indicate, respectively, the minor and major axes at half-power of the elliptical synthesized beam.

### 2.3. Effelsberg 100 m Telescope

Single-point spectra of the four BLAST cores were also obtained with the MPIfR 100 m telescope and its 1.3 cm primary focus receiver. The pointing positions used for the 100 m telescope were different from those used with the VLA and are shown as asterisks in Figures 1–4. Also shown in these figures is the contour representing the half-power width of the 100 m beam. The NH<sub>3</sub>(1,1) and (2,2) lines were observed simultaneously within the same band, in position-switched mode (with a beam throw of 200" along the R.A. direction), with a velocity resolution of 0.077 km s<sup>-1</sup> and  $\sim 10$  minutes of on-source integration time.

The calibration of the 100 m data followed a standard procedure<sup>11</sup> where the arbitrary noise tube units were converted

<sup>10</sup> The National Radio Astronomy Observatory is a facility of the National Science Foundation operated under cooperative agreement by Associated Universities, Inc.

<sup>11</sup> <http://www.mpifr-bonn.mpg.de/div/effelsberg/calibration/calib.html>

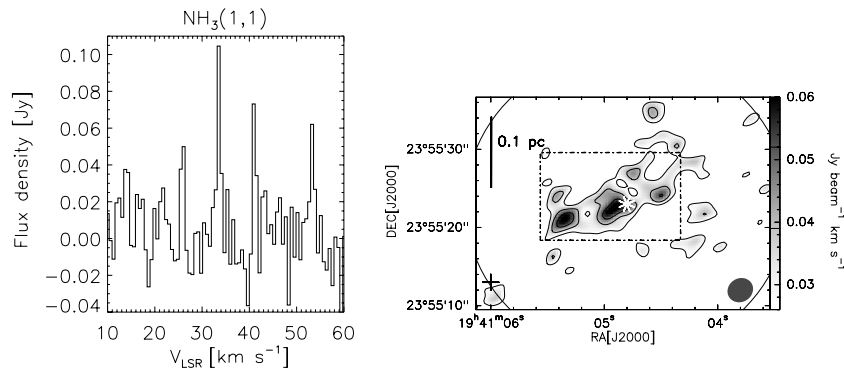


**Figure 1.** V10. Left:  $\text{NH}_3(1,1)$  VLA integrated spectrum of V10. Right: VLA map of the integrated intensity of  $\text{NH}_3(1,1)$  over main and satellite components. The first contour level is at  $+2\sigma$  and the interval between adjacent levels is  $1\sigma$  ( $\text{rms} = 13 \text{ mJy beam}^{-1} \text{ km s}^{-1}$ ). The values corresponding to the contour levels are also indicated by the horizontal lines drawn in the gray-scale wedge to the right. The ellipse in the bottom right-hand corner represents the half-power width of the synthesized beam, while the cross indicates the nominal position of the BLAST core (whose uncertainty is  $\sim 1$  arcmin) and the phase tracking center. The pointing position of the 100 m observations is shown by the asterisk and the large solid circle (only partially visible) represents the half-power width of the 100 m beam. The dot-dashed box represents the area where the line emission has been integrated to generate the spectrum shown in the top panel. The linear scale in the source is shown by the vertical bar in the left-hand side.

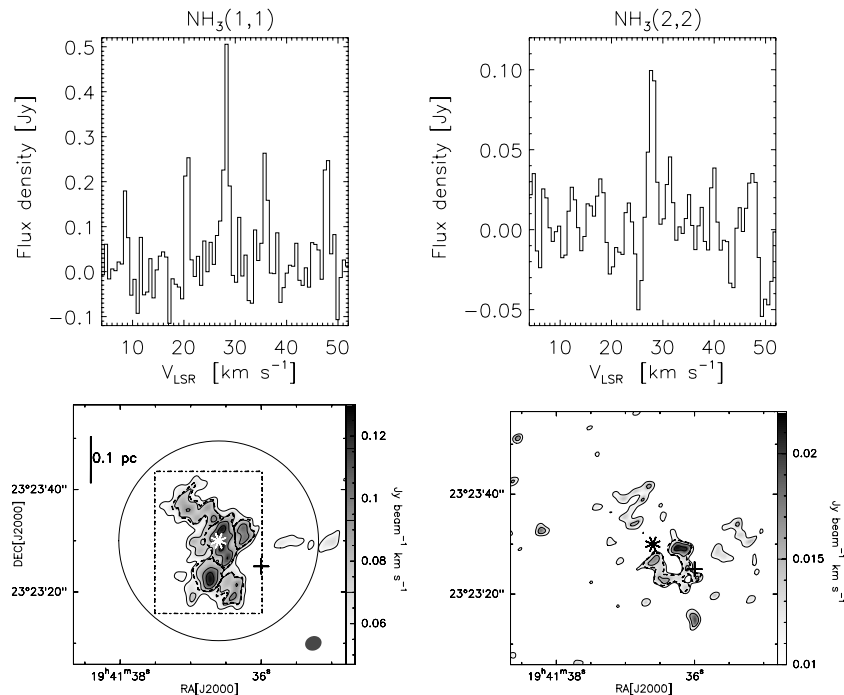


**Figure 2.** V11. Top:  $\text{NH}_3(1,1)$  (left) and  $(2,2)$  (right) VLA integrated spectra of V11. Bottom: VLA maps of the  $\text{NH}_3(1,1)$  (left) and  $(2,2)$  (right) lines, integrated over the main and satellite (in the case of the  $(1,1)$  line) components. The boldface dashed contours in the  $(1,1)$  map indicate the specific sub-regions used to calculate the total mass of the source (see Section 3.3). The boldface dashed contour in the  $(2,2)$  map indicates the region where emission has been averaged to produce the spectrum shown in Figure 15. Other contours and features are as in Figure 1 (with  $\text{rms} = 23 \text{ mJy beam}^{-1} \text{ km s}^{-1}$  and  $5 \text{ mJy beam}^{-1} \text{ km s}^{-1}$  in the  $(1,1)$  and  $(2,2)$  maps, respectively).

to the antenna temperature scale, and both an atmospheric opacity and elevation corrections have been applied to the antenna gain.<sup>12</sup> The main beam efficiency was  $\eta_{\text{mb}} = 0.52$ , the FWHM of the 100 m beam was  $39''$ , and the resulting noise rms in the spectra was  $\sim 100 \text{ mK}$ , corresponding to  $\sim 60 \text{ mJy beam}^{-1}$  (at the native spectral resolution of  $0.077 \text{ km s}^{-1}$ ).

For comparison with the VLA data (Section 2.5), the 100 m spectra were also converted to Jy using the conversion formula

$$S_\lambda (\text{Jy}) = 2.65 \left( \frac{\theta_{\text{mb}} (\text{arcmin})}{\lambda (\text{cm})} \right)^2 T_{\text{mb}}, \quad (2)$$

where  $\theta_{\text{mb}}$  and  $T_{\text{mb}}$  are the main-beam FWHM and brightness temperature, respectively.

#### 2.4. VLA Maps and Spectra

As mentioned earlier, the VLA-D has been used to map the  $\text{NH}_3(1,1)$  and  $(2,2)$  inversion transitions. The corresponding maps and integrated spectra (the integration area is represented by the dot-dashed boxes) are shown in Figures 1–4. Figures 5 and 6 show channel maps of the  $\text{NH}_3(1,1)$  main line toward sources V11 and V27. The  $\text{NH}_3(1,1)$  line has been detected toward all four BLAST cores, whereas the  $(2,2)$  transition has been detected in V11, V27, and V33. This is an excellent result, also because the positional errors of the BLAST sources in

<sup>12</sup> [http://www.mpifr-bonn.mpg.de/staff/tpillai/eff\\_calib/eff\\_calib.html](http://www.mpifr-bonn.mpg.de/staff/tpillai/eff_calib/eff_calib.html)

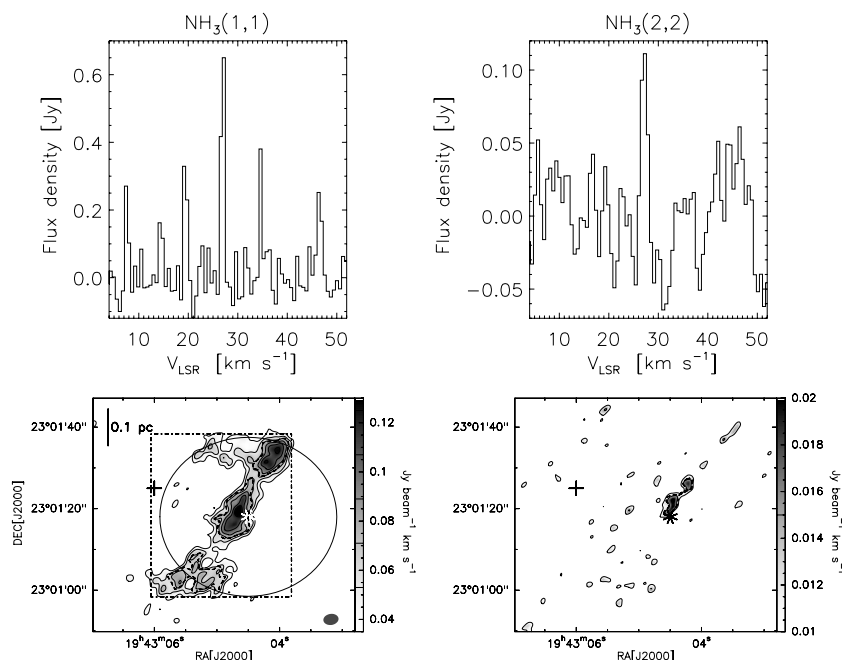


Figure 3. V27. Same as Figure 2 for V27 (with rms = 18 mJy beam<sup>-1</sup> km s<sup>-1</sup> and 5 mJy beam<sup>-1</sup> km s<sup>-1</sup> in the (1,1) and (2,2) maps, respectively).

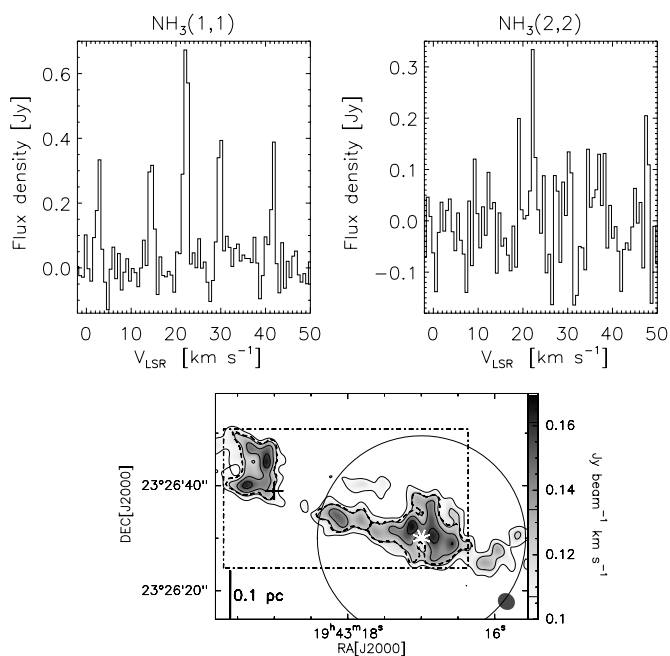


Figure 4. V33. Same as Figure 2 for V33 (with rms = 27 mJy beam<sup>-1</sup> km s<sup>-1</sup> in the (1,1) map), except for the first contour level that here is at 3 $\sigma$ . In the bottom panel only the map of the integrated (1,1) emission is shown (see the text).

Vulpecula, which were estimated by Chapin et al. (2008) to be  $\sim 7''$ – $70''$ , could make these detections more difficult.

We note that in V33 a reliable image of the NH<sub>3</sub>(2,2) emission could not be produced because of the low signal-to-noise ratio (S/N) and extended emission. However, integration of the emission in a box covering most of the NH<sub>3</sub>(1,1) emission yielded a tentative detection of the (2,2) line, as shown in the top right panel of Figure 4. The hyperfine components have been detected only in the (1,1) line. One can note that, in general, the emission appears to arise from a clumpy and filamentary

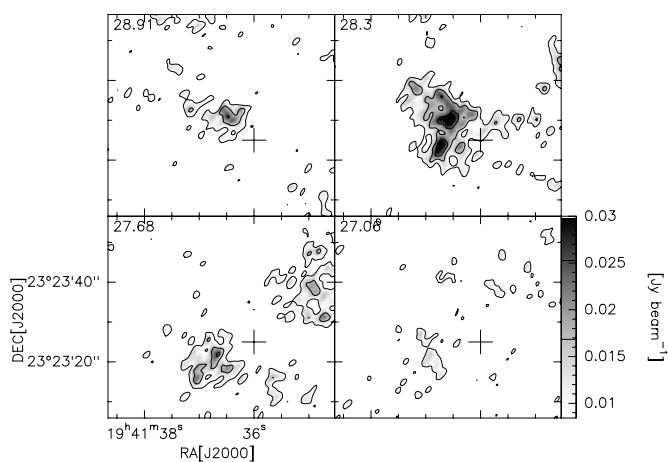


Figure 5. V11. VLA map of NH<sub>3</sub>(1,1) main line toward V11, in four adjacent velocity channels (shown in km s<sup>-1</sup> in the top left corner of each panel). The lowest contour level is 2 $\sigma$ . The cross indicates the nominal position of the BLAST core and the phase tracking center.

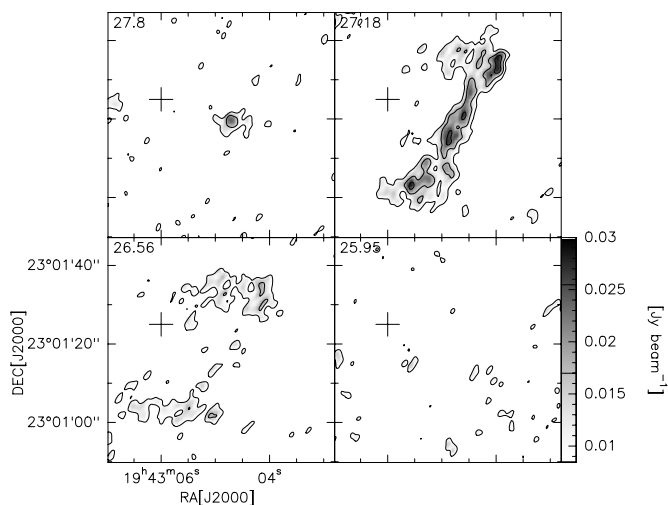
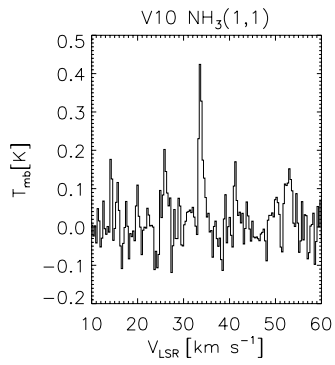
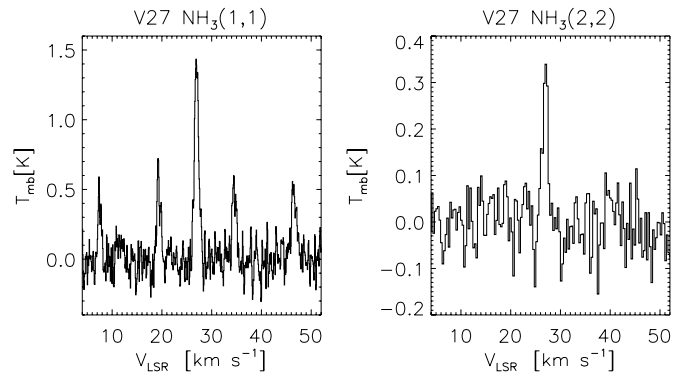


Figure 6. V27. Same as Figure 5 for V27.



**Figure 7.** V10.  $\text{NH}_3(1,1)$  spectrum toward V10 taken with the Effelsberg 100 m telescope. The (2,2) emission was not detected.



**Figure 9.** V27. Same as Figure 8 for V27.

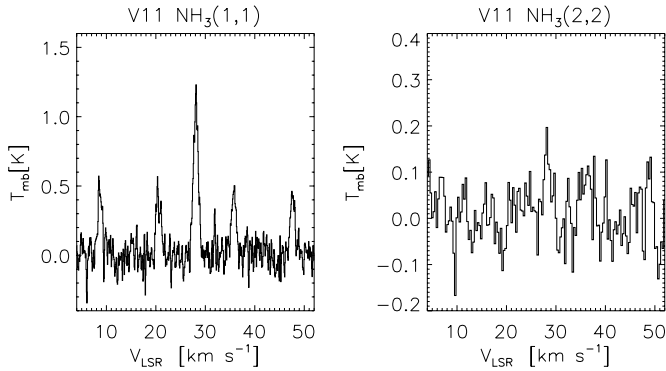


**Figure 8.** V11. Left:  $\text{NH}_3(1,1)$  spectrum toward V11 taken with the Effelsberg 100 m telescope. Right:  $\text{NH}_3(2,2)$  spectrum toward V11 smoothed at a velocity resolution of  $0.3 \text{ km s}^{-1}$ .

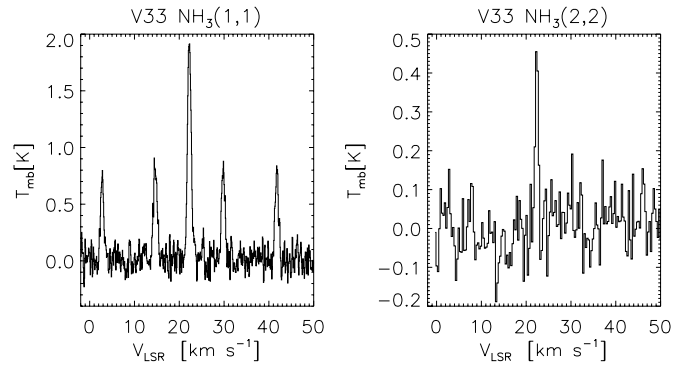


**Figure 10.** V33. Same as Figure 8 for V33.

structure. In V11 and V27 this morphology can be seen even in the weaker (2,2) transition, though at the  $2\sigma$  level.

The velocity scale shown in the spectra of Figures 1–4 (and also in all subsequent spectra) is referred to the  $\text{NH}_3(1,1)$  and (2,2) main lines. We note the excellent agreement with the velocities estimated by Chapin et al. (2008) using  $^{13}\text{CO}(1-0)$ . All spectral lines are clearly very narrow and the VLA observations do not resolve the lines (see later Section 3.1 and Tables 2 and 3). In the case of the (1,1) maps of sources V11 and V27 one can note in Figures 5 and 6 the sharp change in the brightness spatial distribution in adjacent velocity channels. This indicates a significant velocity substructure within  $\sim 1 \text{ km s}^{-1}$ . In V11 and V27 these features are unlikely to be a consequence of missing flux, since with the VLA-D we recover most of the flux measured by the 100 m telescope (see Section 2.5).

Although the morphological difference between these sources could be caused by both intrinsic (e.g., geometrical effects and/or different evolutionary phases) and observational effects, all these cores present very similar features. In fact, they all show an internal structure, with both smaller cores, or fragments, and an inter-core emission, which also appears to be “filamentary.” The fragments inside the cores have sizes  $\lesssim 0.05 \text{ pc}$  and we are unable to resolve structures smaller than  $\simeq 0.034 \text{ pc}$  (7100 AU).

### 2.5. Effelsberg Spectra

The Effelsberg telescope was used to observe the four BLAST sources toward their central positions at higher spectral resolution. The resulting spectra are shown in Figures 7–10, where we note that the hyperfine components of both the inner

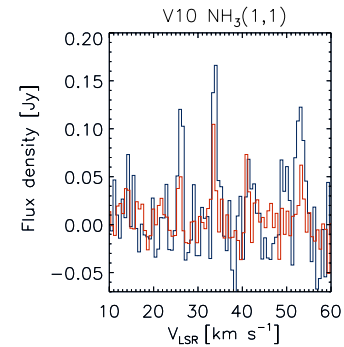


**Figure 11.** V10. Overlay of the  $\text{NH}_3(1,1)$  spectra of Effelsberg (blue line) and VLA (red line) in V10.

(A color version of this figure is available in the online journal.)

and outer satellites are partly resolved, an indication of the narrow linewidths in this source.

For comparison with the VLA, the spectra obtained with the 100 m telescope were resampled at the same spectral resolution as the VLA, and the results are shown in Figures 11–14. The flux measured by the VLA is almost always (exceptions are the  $\text{NH}_3(2,2)$  spectra toward V11 and V33) lower than that observed with the 100 m telescope, probably as a result of both low S/N in the VLA spectra and extended emission that is filtered out by the interferometer. If we compare the main-line emission, the amount of the single-dish flux lost by the VLA varies from  $\simeq 20\%$  to  $30\%$  in V27 and V11 to  $\simeq 50\%$  in V10 and V33. In V11 and V33 the VLA recovers most of the  $\text{NH}_3(2,2)$  single-dish flux.

**Table 2**  
Velocity, Linewidth, and Total Optical Depth from Method NH<sub>3</sub>(1,1)

Source	VLA <sup>a</sup>				100 m			
	$T_{\text{ex}}$ (K)	$V_{\text{lsr}}$ (km s <sup>-1</sup> )	$\Delta V$ (km s <sup>-1</sup> )	$\tau$	$T_{\text{ex}}$ (K)	$V_{\text{lsr}}$ (km s <sup>-1</sup> )	$\Delta V$ (km s <sup>-1</sup> )	$\tau$
V10	4.2 ± 1.2	33.52 ± 0.07	<1.0	1.8 ± 1.0	3.23 ± 0.25	33.69 ± 0.02	0.41 ± 0.05	3.0 ± 0.9
V11	5.0 ± 1.1	28.24 ± 0.04	<1.0	2.0 ± 0.7	3.97 ± 0.27	28.12 ± 0.01	0.83 ± 0.03	2.1 ± 0.3
V27	5.5 ± 2.2	27.00 ± 0.03	<1.0	0.7 ± 0.5	4.63 ± 0.40	26.98 ± 0.01	0.70 ± 0.03	1.6 ± 0.2
V33	4.3 ± 0.4	22.21 ± 0.03	<1.0	2.5 ± 0.4	4.97 ± 0.25	22.26 ± 0.01	0.66 ± 0.02	2.2 ± 0.2

**Note.** <sup>a</sup> The VLA line parameters represent average values, estimated by integrating the NH<sub>3</sub>(1,1) and (2,2) line emission in the dot-dashed boxes shown in Figures 1-4.

**Table 3**  
Results of Gaussian Fits to the NH<sub>3</sub>(2,2) Lines

Source	VLA			100 m		
	$T_{\text{sb}}$ (K)	$V_{\text{lsr}}$ (km s <sup>-1</sup> )	$\Delta V$ (km s <sup>-1</sup> )	$T_{\text{mb}}$ (K)	$V_{\text{lsr}}$ (km s <sup>-1</sup> )	$\Delta V$ (km s <sup>-1</sup> )
V11	0.46 ± 0.09	27.91 ± 0.13	1.4 ± 0.3	0.16 ± 0.06	28.23 ± 0.19	1.44 ± 0.56
V27	0.24 ± 0.06	27.13 ± 0.15	1.3 ± 0.3	0.33 ± 0.06	26.96 ± 0.08	1.23 ± 0.18
V33	0.62 ± 0.14	22.27 ± 0.13	<1.0	0.52 ± 0.09	22.36 ± 0.04	0.72 ± 0.08

**Note.** The VLA fits have been performed on the integrated spectra in the area shown by the dot-dashed boxes in Figures 2-4.

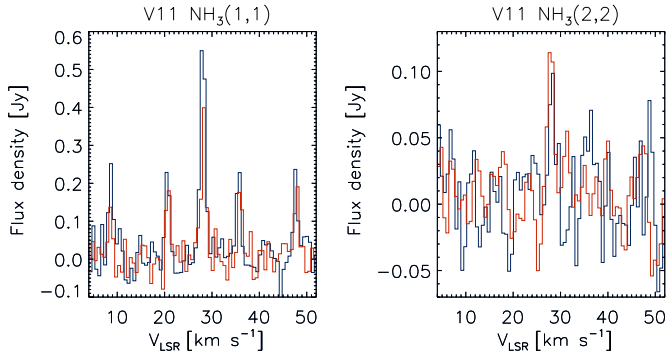


**Figure 12.** V11. Left: overlay of the NH<sub>3</sub>(1,1) spectra of Effelsberg (blue line) and VLA (red line) in V11. Right: same as above for NH<sub>3</sub>(2,2).  
(A color version of this figure is available in the online journal.)

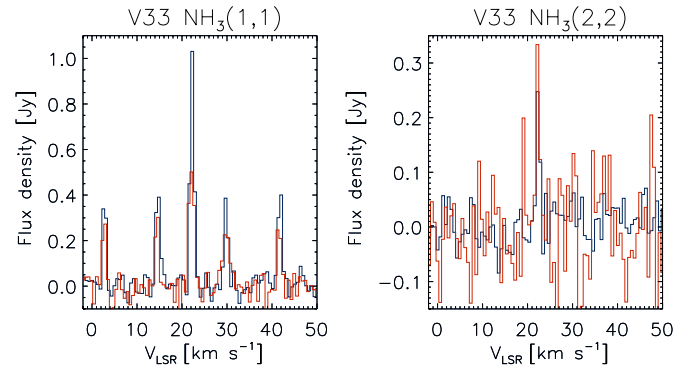


**Figure 14.** V33. Same as Figure 12 for V33.  
(A color version of this figure is available in the online journal.)

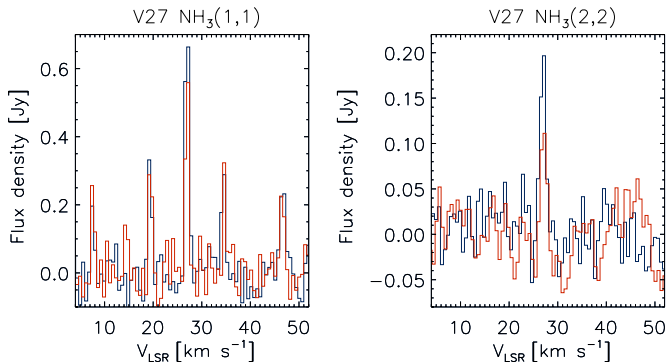


**Figure 13.** V27. Same as Figure 12 for V27.  
(A color version of this figure is available in the online journal.)

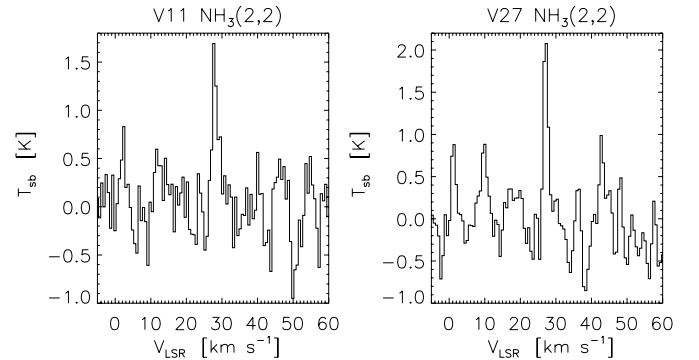


**Figure 15.** NH<sub>3</sub>(2,2) VLA spectra toward V11 (left panel) and V27 (right panel), obtained by integrating the emission within the boldface dashed contours shown in the (2,2) maps of Figures 2 and 3.

### 3. ANALYSIS

#### 3.1. Derivation of Physical Parameters with METHOD NH<sub>3</sub>(1,1)

The NH<sub>3</sub>(1,1) and (2,2) inversion lines show an electric quadrupole and magnetic hyperfine structure (see Ho & Townes 1983 for a review). The (1,1) spectra were fitted using a

non-linear least-square method (METHOD NH<sub>3</sub>(1,1) of the CLASS program) which takes into account the 18 hyperfine components. This method can determine the optical depths and linewidths assuming that all components have equal excitation temperatures, that the line separation is fixed at the laboratory value, and that the linewidths are identical.

**Table 4**  
Temperature and Column Density

Source	VLA <sup>a</sup>			100 m		
	$T_{12}$ (K)	$T_k$ (K)	$N(\text{NH}_3)$ ( $\times 10^{14} \text{ cm}^{-2}$ )	$T_{12}$ (K)	$T_k$ (K)	$N(\text{NH}_3)$ ( $\times 10^{14} \text{ cm}^{-2}$ )
V11	$10.5 \pm 0.5$	$11.1 \pm 0.6$	$21.5 \pm 4.7$	$11.9 \pm 1.1$	$12.8 \pm 1.3$	$6.6 \pm 1.0$
V27	$8.7 \pm 0.5$	$9.0 \pm 0.6$	$34.1 \pm 8.4$	$14.3 \pm 0.6$	$16.0 \pm 1.0$	$3.9 \pm 0.4$
V33	$9.2 \pm 0.2$	$9.5 \pm 0.2$	$37.8 \pm 6.7$	$12.2 \pm 0.3$	$13.1 \pm 0.5$	$6.5 \pm 0.4$

**Note.** <sup>a</sup> The VLA line parameters represent average values, estimated by integrating the  $\text{NH}_3(1,1)$  within the sub-regions enclosed by the dashed contours in Figures 2–4 (see the text and Figure 16).

The  $\text{NH}_3(2,2)$  lines are weaker and the sensitivity of these observations is less than the sensitivity of the  $\text{NH}_3(1,1)$  data. Thus, the quadrupole hyperfine structure of the  $\text{NH}_3(2,2)$  transition is not visible when the emission is averaged over the same large area as the (1,1) line, shown by the dot-dashed boxes in Figures 1–4. The hyperfine structure of the (2,2) line becomes visible in sources V11 and V27 (see Figure 15) only when the emission is averaged on smaller sub-regions, such as the ones shown by the boldface dashed contours in Figures 2 and 3. Therefore, for the purpose of using METHOD  $\text{NH}_3(1,1)$  of the CLASS program we always fitted the (2,2) profiles (obtained by integrating the VLA maps in the same region as the (1,1) transition) by simple Gaussians. Due to the hidden magnetic hyperfine structure, this tends to overestimate the intrinsic linewidths (Bachiller et al. 1987).

The results of the  $\text{NH}_3(1,1)$  fitting are listed in Table 2. The 100 m spectra have the advantage of a better S/N and spectral resolution and therefore the derived parameters are more accurate, though they do not necessarily describe the same volume of gas. The effect of the better spectral resolution is clearly visible in the resulting linewidths (see Table 2). As mentioned earlier the VLA does not resolve the lines and thus the VLA linewidths should be interpreted only as upper limits. On the other hand, the 100 m results show that the linewidths are indeed different and very narrow. A temperature of  $T_k = 14 \text{ K}$  corresponds to an  $\text{NH}_3$  thermal linewidth of  $\Delta V_{\text{th}} = 0.19 \text{ km s}^{-1}$  ( $\Delta V_{\text{th}} = \sqrt{8 \ln 2 k T_k / (17 m_{\text{H}})}$ , where  $k$  is the Boltzmann constant and  $m_{\text{H}}$  is the atomic hydrogen mass). Therefore, non-thermal motions definitely give an important contribution in these sources. The overall linewidths, however, are smaller (or much smaller in the case of V10) than those previously observed toward (warmer) HMPOs by, e.g., Molinari et al. (1996), who found median linewidths  $\simeq 1.7\text{--}1.8 \text{ km s}^{-1}$ , and also by Motte et al. (2007) who found linewidths  $\gtrsim 2.0 \text{ km s}^{-1}$ .

Source V11 has the largest linewidth, as measured by both (1,1) and (2,2) lines. We also note that V11 is the only source where the velocity structure shown in Figure 5 is suggesting the presence of either two cores at separate velocities or a velocity gradient, positive S to N, of  $\simeq 11 \text{ km s}^{-1} \text{ pc}^{-1}$ . Neither of these can be ruled out on the basis of the present data. Incidentally, V11 is also the only source with a clear positional association with a likely protostar (see Section 3.5).

The results of the Gaussian fits to the  $\text{NH}_3(2,2)$  profiles are listed in Table 3. Because the Gaussian fit does not take into account the hyperfine structure of the line, we cannot compare directly the linewidths in Tables 2 and 3. We also note the same basic behavior among those sources with a (2,2) detection: source V33 has in fact the smallest linewidth as

measured by both (1,1) and (2,2) lines. However, because in the VLA spectrum the (2,2) line is barely two channels wide (see Figure 14), in Table 3 we only list an upper limit.

### 3.2. Temperature

In V11, V27, and V33, where the (2,2) line was detected, we were also able to determine the rotation temperature,  $T_{12}$  (and thus the kinetic temperature  $T_k$ ), and the column density using the method of Ungerechts et al. (1986) and Bachiller et al. (1987). In this method the required data were (1) the product  $\tau(T_{\text{ex}} - T_{\text{bg}})$  for the (1,1) line, where  $T_{\text{ex}}$  and  $T_{\text{bg}} = 2.725 \text{ K}$  are the excitation and background temperatures, respectively, and  $\tau$  is the optical depth; (2) the linewidth  $\Delta V(1,1)$ ; and (3) the (2,2) integrated intensity. Once  $T_{12}$  has been estimated, the kinetic temperature can be determined using the analytical expression of Tafalla et al. (2004):

$$T_k = \frac{T_{12}}{1 - \frac{T_{12}}{42} \ln \left[ 1 + 1.1 \exp \left( -\frac{16}{T_{12}} \right) \right]}, \quad (3)$$

which is an empirical expression that fits the  $T_{12} - T_k$  relation obtained using a radiative transfer model.

The results are shown in Table 4. The VLA physical parameters represent average values, estimated by first integrating the  $\text{NH}_3(1,1)$  in the smaller sub-regions enclosed by the boldface dashed contours shown in Figures 2–4 (see also Section 3.3); then, the parameters obtained in each of these sub-regions have been averaged together and the results listed in Table 4. Because of the coarse spectral resolution of the VLA spectra, when evaluating the physical parameters from the VLA data we have replaced the original linewidths with the 100 m linewidths. Although the 100 m linewidths represent themselves averages over a larger source area compared to the smaller sub-regions shown in Figures 2–4, they give a better estimate of the  $\Delta V(1,1)$  values as compared to the upper limits given by the VLA linewidths. In addition, because of the weakness of the (2,2) transition, we could not obtain separate (2,2) integrated spectra for the sub-regions. As a consequence, we have always used the  $\text{NH}_3(2,2)$  spectrum obtained by integrating over the entire source, as shown in Figures 2–4.

The small linewidths listed in Table 2 and the low kinetic temperatures of Table 4 again suggest small internal motions and therefore very quiescent conditions. The four BLAST cores appear to be even colder and more quiescent than the HMSC candidates observed by Sridharan et al. (2005), who found in their sample of candidate HMSCs a median linewidth of  $1.5 \text{ km s}^{-1}$ , comparable with that of Molinari et al. (1996), and a median rotation temperature of 16.9 K. The average

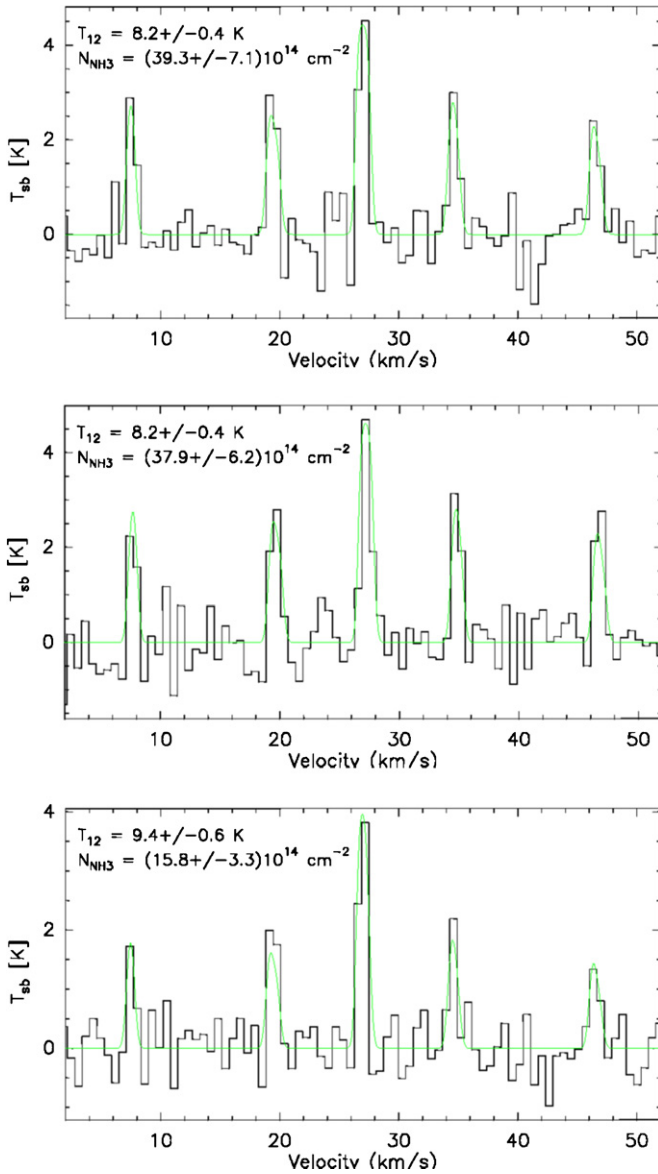


**Figure 16.** VLA spectra obtained toward V27 by selecting the three smaller sub-regions enclosed by the boldface dashed contours shown in Figure 3. The solid line represents the fit obtained with METHOD NH<sub>3</sub>(1,1) of the CLASS program, by setting the VLA linewidths to the 100 m values (see the text). Also shown are the values of the rotation temperature (Section 3.2) and NH<sub>3</sub> column density as obtained in each separate sub-region (see Section 3.3 and Table 4, where the parameters listed are weighted averages).

(A color version of this figure is available in the online journal.)

temperature of our cores is also somewhat lower than the mean kinetic temperature of 15 K found in IRDCs by Pillai et al. (2006).

### 3.3. Column Density and Mass

The three fitting parameters described in Section 3.2 may also be used to determine the column densities,  $N(1,1)$  and  $N(2,2)$ , of the (1,1) and (2,2) lines. Then, the total NH<sub>3</sub> column density,  $N_{\text{NH}_3}$ , is obtained from  $T_{12}$  using the method of Ungerechts et al. (1986). The total mass in the VLA maps has been estimated by dividing each source into smaller sub-regions (shown by the boldface dashed contours in Figures 2–4) and determining  $N_{\text{NH}_3}$  in each of them. The approximate size of each region represents a trade-off between the need to achieve a good S/N in the integrated spectra of each region, and the need to avoid

integrating over too large an area with no NH<sub>3</sub> emission. For the VLA data, the values of temperatures and column densities averaged in these sub-regions in sources V11, V27, and V33 are listed in Table 4.

As an example of the NH<sub>3</sub>(1,1) spectra and line fits obtained with this procedure we show in Figure 16 the spectra obtained toward V27 by integrating the emission in the three smaller areas, enclosed within dashed contours, shown in Figure 2. As mentioned already in Section 3.2, for each sub-region we have used the same NH<sub>3</sub>(2,2) spectrum obtained by integrating over the entire source. In addition, the NH<sub>3</sub>(1,1) linewidths have been kept fixed, and equal to the 100 m values, during the fits to the VLA spectra obtained using METHOD NH<sub>3</sub>(1,1) of CLASS, such as the ones shown Figure 16. The total mass of each source can then be computed by adding the masses of the individual sub-regions, estimated as

$$M_{\text{cd}} = 1.38 \frac{\pi}{4} D^2 N_{\text{H}_2} m_{\text{H}_2}, \quad (4)$$

where  $D$  is the sub-region diameter,  $m_{\text{H}_2}$  is the mass of the H<sub>2</sub> molecule,  $N_{\text{H}_2}$  is the sub-region averaged column density, and 1.38 is the correction factor for the abundance of helium and heavier elements in the interstellar medium. The source diameter is actually an equivalent diameter calculated as  $\sqrt{\Omega_s/1.133}$ , where  $\Omega_s$  represents the solid angle covered by the individual sub-regions shown in Figures 2–4. We have evaluated  $M_{\text{cd}}$  for two possible values of the ammonia abundance, corresponding to the minimum and maximum values found in Table 3 of Pillai et al. (2006),  $X[\text{NH}_3] = 7 \times 10^{-9}$  and  $X[\text{NH}_3] = 10^{-7}$ . The corresponding values of  $M_{\text{cd}}$  are listed separately in Table 5 (Columns 6 and 7). The particle density has then been calculated as

$$n_{\text{H}_2} = \frac{3M_{\text{cd}}}{4\pi(D/2)^3 \mu m_{\text{H}}}, \quad (5)$$

where  $\mu = 2.33$  is the mean molecular weight per particle and  $m_{\text{H}}$  is the mass of the hydrogen atom. The two values of  $n_{\text{H}_2}$  corresponding to the choice of  $X[\text{NH}_3]$  are also listed separately in Table 5 (Columns 8 and 9).

From the linewidths of the observed transitions and the estimated source angular diameters we can also derive the mass required for virial equilibrium. Assuming the source to be spherical and homogeneous (an assumption which is not, however, well justified in all of our sources), and neglecting contributions from magnetic field and surface pressure, the virial mass is given by MacLaren et al. (1988):

$$M_{\text{vir}}(M_{\odot}) = 0.509 d(\text{kpc}) \theta_s(\text{arcsec}) (\Delta V(\text{km s}^{-1}))^2, \quad (6)$$

where  $d = 2.3$  kpc (Chapin et al. 2008) is the distance to the four BLAST sources. The estimated virial masses (Column 5 in Table 5) show that the cores more likely to be gravitationally unstable, even when the largest value of  $X[\text{NH}_3] = 10^{-7}$  is used, are V33 and, to a lesser extent, V27. Source V11 seems to be closer to virial equilibrium, compared to V27 and V33, which would appear to be consistent with V11 being a proto-stellar core (see Section 3.5). For comparison, the virial masses listed in Table 5 are quite smaller compared to the values estimated by Fontani et al. (2004) for comparable sizes. However, these authors did not use their NH<sub>3</sub> map and spectra to determine the virial mass, and they measured much larger linewidths in other molecular tracers. Therefore, the virial masses of Fontani et al. (2004) are likely to reflect the much larger degree of turbulence in HMPOs.

**Table 5**  
Size, Mass, and Density

Source	Diameter <sup>a</sup>		$M_{\text{BLAST}}^b$	$M_{\text{vir}}$	$M_{\text{tot}}^c$		$\langle n_{\text{H}_2} \rangle^c$	
	(arcsec)	(pc)			( $M_{\odot}$ )	( $M_{\odot}$ )	( $\times 10^5 \text{ cm}^{-3}$ )	( $\times 10^5 \text{ cm}^{-3}$ )
V10	7.6	0.08	89	1.5	...	...	...	...
V11	12.6	0.14	213	10.2	5.0	72.0	2.2	31.0
V27	11.6	0.13	105	6.7	9.7	138.5	2.3	33.4
V33	18.8	0.21	107	9.6	21.0	300.7	2.1	30.0

**Notes.**  $M_{\text{tot}}$  represents the total mass of the source as estimated by summing the masses ( $M_{\text{cd}}$ ) of the sub-regions enclosed by dashed contours shown in Figures 2–4.  $\langle n_{\text{H}_2} \rangle$  represents the average density among the sub-regions in which each source has been divided.

<sup>a</sup> Estimated from the total area of the source within the 50% contour.

<sup>b</sup> BLAST core masses from Chapin et al. (2008).

<sup>c</sup> The first and second value of both  $M_{\text{tot}}$  and  $\langle n_{\text{H}_2} \rangle$  correspond to the values of  $X[\text{NH}_3] = 10^{-7}$  and  $X[\text{NH}_3] = 7 \times 10^{-9}$ , respectively. The errors on  $M_{\text{tot}}$  are derived from the errors on  $N_{\text{H}_2}$  for each separate region, and vary between  $\simeq 15\%$  and  $25\%$ .

Furthermore, apart from the various approximations involved in the calculation of  $M_{\text{vir}}$ , its comparison with the masses obtained by the fit to the spectral energy distribution (with assumed values of the dust mass absorption coefficient at  $250 \mu\text{m}$ ,  $k_{250} = 10 \text{ cm}^2 \text{ g}^{-1}$ , and a dust emissivity index,  $\beta = 1.5$ ; Chapin et al. 2008) is further complicated by the fact that the BLAST 05 observations were sensitive to cold dust on a much larger scale ( $\gtrsim 1$  arcmin).

The comparison between  $M_{\text{tot}}$  and  $M_{\text{vir}}$  in Table 5 is complicated by the many uncertainty factors. In addition, for a power-law density distribution of the type  $n_{\text{H}_2}(r) \propto r^{-m}$ , the virial mass obtained from Equation (6) must be multiplied by a factor  $\frac{3}{5} \frac{5-2m}{3-m}$  (see MacLaren et al. 1988). For example, Fontani et al. (2004) found that  $m = 2.3$  in the HMPO IRAS 23385+6053 and thus their virial masses had to be multiplied by a factor  $\simeq 0.35$ .

### 3.4. Comparison with Low-mass Pre-stellar Cores

To analyze the origin of the V10, V11, V27, and V33 cores, we can compare the properties of these cores with the well-studied low-mass pre-stellar core L1544 in the Taurus molecular cloud (at a distance of 140 pc) that appears to be gravitationally unstable (for a review, see Doty et al. 2005 and references therein). The L1544 core has a continuum source with a flux density of  $17.4 \text{ Jy}$  at  $450 \mu\text{m}$  (Shirley et al. 2000), corresponding to a gas+dust mass of  $3.2 M_{\odot}$ , and a density of  $1.5 \times 10^6 \text{ cm}^{-3}$  (Ward-Thompson et al. 1999). The  $\text{N}_2\text{H}^+$  linewidth toward L1544 is  $0.3 \text{ km s}^{-1}$ , and observations toward several low-mass starless cores in  $\text{NH}_3$  and  $\text{N}_2\text{H}^+$  show similar linewidths for both molecules (Tafalla et al. 2004).

In order to compare the physical properties of L1544 with those of the BLAST cores listed in Table 5, we note that the peak  $\text{NH}_3$  abundance determined by Tafalla et al. (2002) toward L1544 was  $4.0 \times 10^{-9}$ . Therefore, if we consider the physical parameters in Table 5 corresponding to the lower value of the  $\text{NH}_3$  abundance ( $7.0 \times 10^{-9}$ , close enough to that estimated in L1544), we see that the number density in the BLAST cores is quite similar to that of L1544, while their mass is a factor of  $\sim 20$ – $100$  higher, and is quite higher even when one considers the masses of the smaller sub-regions within each source, as described in Section 3.3.

As far as the velocity dispersion is concerned, the BLAST cores have  $\text{NH}_3$  linewidths more than double that of L1544, with the exception of V10 which has a linewidth ( $0.41 \text{ km s}^{-1}$ ; see Table 2) only slightly higher than that of L1544. This would

be consistent with the BLAST cores being more turbulent and could also possibly hide other systematic internal motions (see the case of V11, Section 3.1).

What would a core like L1544 appear in the BLAST 05 map of Vulpecula? Scaling the  $450 \mu\text{m}$  L1544 emission to  $500 \mu\text{m}$  at a distance of 2.3 kpc, we would expect an integrated flux density of about 40 mJy and thus it would go undetected in the BLAST 05 map of Vulpecula (Chapin et al. 2008). This is consistent with the four BLAST sources being separated, if they were plotted on the  $L$ – $M$  diagram of Molinari et al. (2008), from the low-mass regime, as mentioned in Section 2.1.

Table 5 shows that only in the case of V11 the total mass inferred from the BLAST observations is significantly larger than the mass estimate based on  $\text{NH}_3$  emission, given the  $\text{NH}_3$  abundance range that we have selected. In V27 and V33, the mass range obtained from our observations is consistent with the BLAST mass estimate. It is possible that in the case of V11 the ammonia emission results from only a small fraction of molecular material that is concentrated in a denser and more compact structure. A similar scenario, for example, has been found by Shepherd et al. (2004) toward the core G192 S3, and it could also be the case in V27 and V33 if the  $\text{NH}_3$  abundance were near the upper limit of the range listed in Table 5. In this case, an interesting question would be whether the mass determined from the VLA  $\text{NH}_3$  observations represents the total reservoir from which any star formation will eventually take place in these cores or, rather, further mass will be accreted from the larger mass reservoir detected by BLAST. In the first scenario, it is unlikely that these cores will produce massive stars, unless the total gas and dust mass is much higher, as it would result if  $X[\text{NH}_3] \ll 10^{-7}$ .

Likewise, one might ask whether the lower-mass fragments in these regions could at a later stage merge to form a more massive pre-stellar core that could then evolve toward a high-mass star. Clearly, we cannot currently determine the relative motions of the individual fragments in the observed cores. However, we can use the  $\text{NH}_3$  linewidths as a rough estimate of the average turbulent motion, though they do not necessarily represent the relative velocities of coherent sub-structures within the cores. If we take  $\sim 0.1 \text{ pc}$  and  $0.8\sqrt{3} \text{ km s}^{-1}$  as the typical fragment (de-projected) separation and three-dimensional velocity dispersion, respectively, we obtain a timescale  $\sim 8 \times 10^4 \text{ yr}$ . Although this timescale is comparable to the accretion timescales estimated by Bonnell & Bate (2006) for the formation of high-mass stars in the competitive accretion scenario, the most significant

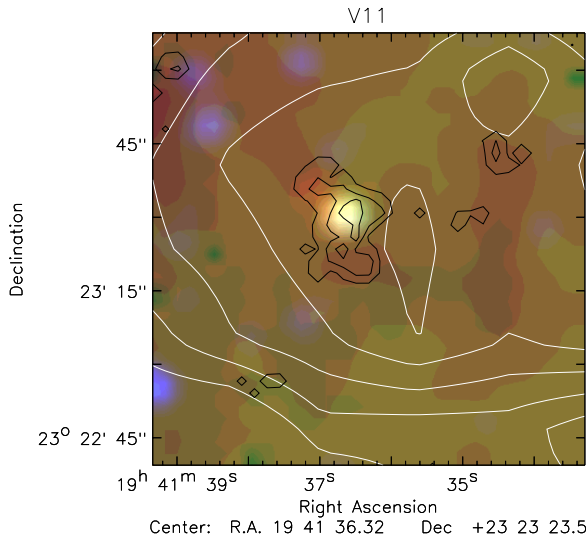


**Figure 17.** Three-color *Spitzer* image 3.6  $\mu\text{m}$  (blue), 8  $\mu\text{m}$  (green), and 24  $\mu\text{m}$  (red) of V11 (at the angular resolution of the MIPS 24  $\mu\text{m}$  map). The overlaid white, solid contours represent the BLAST 350  $\mu\text{m}$  emission (from  $4.3 \times 10^7$  to  $1.2 \times 10^8$  by  $1.6 \times 10^7$   $\text{Jy srad}^{-1}$ ). The black, solid contours represent the integrated  $\text{NH}_3(1,1)$  VLA emission (from 0.039 to 0.112 by  $0.036$   $\text{Jy beam}^{-1} \text{ km s}^{-1}$ ).

(A color version of this figure is available in the online journal.)

individual fragments inside the cores appear to be more massive than the thermal Jeans mass ( $\sim 1 M_{\odot}$ ), which is inconsistent with the model of Bonnell & Bate (2006) for competitive accretion. Alternatively, it is quite possible that we are observing these cores at a phase when merging of low-mass fragments has already occurred, and that the less significant fragments in Figures 1–4, with masses  $\gtrsim 1 M_{\odot}$ , are actually the remnants of this accreting phase.

### 3.5. Evolutionary Phase of the Cores

As we have seen in Sections 3.2 and 3.3, our cores have similar temperatures but are more compact, and possibly less massive (depending on the  $\text{NH}_3$  abundance), than IRDCs, which have a typical size  $\gtrsim 1$  pc. This suggests that they may be similar to the unresolved cores found toward IRDCs, but in an earlier stage of evolution compared to the sources observed by Molinari et al. (1996) and Sridharan et al. (2005).

This conclusion is supported by the lack of an *IRAS* and *MSX* counterpart to these sources, as mentioned in Section 2.1. However, we have also inspected the *IRAC* and *MIPS* images and found that only in the case of V11 an *IRAC*/*MIPS* point source is found to be positionally coincident with the  $\text{NH}_3(1,1)$  integrated emission. As shown in Figure 17 this source has the colors expected for an embedded protostar. Aperture photometry confirms that the SED of this infrared source is rising between 3.6 and 24  $\mu\text{m}$ . However, we find no point source in the 70  $\mu\text{m}$  *MIPS* image. No other infrared source with similar colors is found within  $\simeq 1$  arcmin from the peak of either the  $\text{NH}_3(1,1)$  or the BLAST emission. Together with the larger linewidth and a more systematic velocity shift across the source structure, as discussed in Section 3.1, these properties suggest that V11 is probably the most evolved of all four observed cores, and is likely to harbor a protostar.

In addition, we have also searched for possible radio continuum emission toward the four Vulpecula sources. In order to do this we have analyzed both the continuum images constructed from the line-free channels of our VLA observations, and the

available maps from the CORNISH survey of the Galactic Plane (Purcell et al. 2008). We do not detect any continuum emission at the level of  $\simeq 0.4$   $\text{mJy beam}^{-1}$ , in our line-free channels maps, which is about the same as the noise level achieved at 5 GHz in the CORNISH maps. Thus, both the upper limit to the continuum emission (see Purcell et al. 2008) and the luminosity estimated from SED fits ( $L \sim 50 L_{\odot}$ ; Chapin et al. 2008) imply an ionizing source much less than a B3 zero-age main-sequence star. The low luminosity in the radio continuum could be because the central object has not yet developed a UC H II region, or because of opacity if the surroundings of the protostar (if any) are very dense.

## 4. CONCLUSIONS

We have observed four candidate high-mass starless cores selected from the BLAST 05 survey of the Vulpecula region. Our VLA-D observations in the  $\text{NH}_3(1,1)$  and (2,2) lines suggest that these cores are in very early stages of evolution, prior to the formation of a (proto)star or proto-cluster. In only one of these cores, V11, the VLA peak emission of  $\text{NH}_3(1,1)$  is associated with an infrared source having the colors expected for an embedded protostar. The four cores are cold ( $T_{\text{k}} < 16$  K), relatively quiescent ( $\Delta V \lesssim 0.8$   $\text{km s}^{-1}$ ) but with a higher velocity dispersion compared to, e.g., L1544, and show a filamentary and clumpy structure. Our VLA-D data have limited spectral resolution, but we can clearly observe a significant velocity substructure within  $\sim 1$   $\text{km s}^{-1}$ .

Based on the comparison with a typical low-mass pre-stellar core, we find that these BLAST cores are more massive and more luminous. V11 is likely to have already formed an intermediate-mass (proto)star and given the mass range obtained for V27 and V33 they too could form intermediate- or even high-mass stars. However, a confirmation of this conclusion will require a more accurate determination of the  $\text{NH}_3$  abundance in these cores.

The authors thank R. Cesaroni and A. Lopez Sepulcre for kindly providing the 100 m data. L.O. and C.M.P. acknowledge travel support from NRAO during their stay at the Array Operations Center in Socorro (NM). P.H. acknowledges partial support from NSF grant AST-0908901. P.G.M. acknowledges partial support from NSERC. The authors also wish to thank an anonymous referee whose comments have considerably improved the paper.

## REFERENCES

- Aikawa, Y., Herbst, E., Roberts, H., & Caselli, P. 2005, *ApJ*, 620, 330  
 Bachiller, R., Guilloteau, S., & Kahane, C. 1987, *A&A*, 173, 324  
 Benjamin, R. A., et al. 2003, *PASP*, 115, 953  
 Beuther, H., Schilke, P., Menten, K. M., Motte, F., Sridharan, T. K., & Wyrowski, F. 2002, *ApJ*, 566, 945  
 Bonnell, I. A., & Bate, M. R. 2006, *MNRAS*, 370, 488  
 Bontemps, S., Motte, F., Csengeri, T., & Schneider, N. 2009, arXiv:0909.2315  
 Chapin, E., et al. 2008, *ApJ*, 681, 428  
 Cyganowski, C. J., et al. 2008, *AJ*, 136, 2391  
 Doty, S. D., Everett, S. E., Shirley, Y. L., Evans, N. J., & Palotti, M. L. 2005, *MNRAS*, 359, 228  
 Flower, D. R., Pineau Des Forêts, G., & Walmsley, C. M. 2006, *A&A*, 456, 215  
 Fontani, F., Zhang, Q., Caselli, P., & Bourke, T. L. 2009, *A&A*, 499, 233  
 Fontani, F., et al. 2004, *A&A*, 414, 299  
 Ho, P. T. P., & Townes, C. H. 1983, *ARA&A*, 21, 239  
 MacLaren, I., Richardson, K. M., & Wolfendale, A. W. 1988, *ApJ*, 333, 821  
 Molinari, S., Brand, J., Cesaroni, R., & Palla, F. 1996, *A&A*, 308, 573  
 Molinari, S., Pezzuto, S., Cesaroni, R., Brand, J., Faustini, F., & Testi, L. 2008, *A&A*, 481, 345  
 Molinari, S., Testi, L., Rodríguez, L. F., & Zhang, Q. 2002, *ApJ*, 570, 758

- Motte, F., Bontemps, S., Schilke, P., Schneider, N., Menten, K. M., & Broguière, D. 2007, *A&A*, **476**, 1243
- Pascale, E., et al. 2008, *ApJ*, **681**, 400
- Pillai, T., Wyrowski, F., Carey, S. J., & Menten, K. M. 2006, *A&A*, **450**, 569
- Purcell, C. R., Hoare, M. G., & Diamond, P. 2008, in ASP Conf. Ser. 387, *Massive Star Formation: Observations Confront Theory*, ed. H. Beuther, H. Linz, & T. Henning (San Francisco, CA: ASP), 389
- Shepherd, D. S., Borders, T., Claussen, M., Shirley, Y., & Kurtz, S. 2004, *ApJ*, **614**, 211
- Shirley, Y. L., Evans, II, N. J., Rawlings, J. M. C., & Gregersen, E. M. 2000, *ApJS*, **131**, 249
- Sridharan, T. K., Beuther, H., Saito, M., Wyrowski, F., & Schilke, P. 2005, *ApJ*, **634**, L57
- Sridharan, T. K., Beuther, H., Schilke, P., Menten, K. M., & Wyrowski, F. 2002, *ApJ*, **566**, 931
- Tafalla, M., Myers, P. C., Caselli, P., & Walmsley, C. M. 2004, *A&A*, **416**, 191
- Tafalla, M., Myers, P. C., Caselli, P., Walmsley, C. M., & Comito, C. 2002, *ApJ*, **569**, 815
- Ungerechts, H., Winnewisser, G., & Walmsley, C. M. 1986, *A&A*, **157**, 207
- Wang, Y., Zhang, Q., Pillai, T., Wyrowski, F., & Wu, Y. 2008, *ApJ*, **672**, L33
- Ward-Thompson, D., Motte, F., & André, P. 1999, *MNRAS*, **305**, 143
- Zhang, Q., Wang, Y., Pillai, T., & Rathborne, J. 2009, *ApJ*, **696**, 268
- Zinnecker, H., & Yorke, H. W. 2007, *ARA&A*, **45**, 481